SCIENCE CHINA
Chemistry

•ARTICLES•

December 2019 Vol.62 No.12: 1704–1709
https://doi.org/10.1007/s11426-019-9624-x

Atomic-scale imaging of the defect dynamics in ceria nanowires under heating by *in situ* aberration-corrected TEM

Xiaomin Li[1], Kaihui Liu[1*], Wenlong Wang[2,3] & Xuedong Bai[2,3,4*]

[1]*International Center for Quantum Materials and School of Physics, Peking University, Beijing 100871, China;*
[2]*Beijing National Laboratory for Condensed Matter Physics, Institute of Physics, Chinese Academy of Sciences, Beijing 100190, China;*
[3]*Songshan Lake Materials Laboratory, Dongguan 523808, China;*
[4]*School of Physical Science, University of Chinese Academy of Sciences, Beijing 100049, China*

Received August 7, 2019; accepted September 24, 2019; published online November 6, 2019

The defects in the ceria usually work as the active reaction sites in their industrial applications. In this article, we studied the formation and atomic process of the defects of ceria nanowires under heating by using *in situ* aberration-corrected transmission electron microscopy (Cs-TEM) method. With the temperature elevating, ceria nanowires are reduced and defects begin to appear and grow up. When temperature reaches 1,023 K, the defect morphology exhibits the rhombus or hexagon patterns, which are surrounded by {111} and {200} planes with lower surface energy, and the heated ceria still maintain the same cubic fluorite structure as their parent. It is also indicated that the formation of defects originates from the release of lattice oxygen and the volatilization of surface Ce ions. This work provides an important insight into designing ceria-based catalysts and ionic conductors.

ceria, defects, heating, *in situ* transmission electron microscopy

Citation: Li X, Liu K, Wang W, Bai X. Atomic-scale imaging of the defect dynamics in ceria nanowires under heating by *in situ* aberration-corrected TEM. *Sci China Chem*, 2019, 62: 1704–1709, https://doi.org/10.1007/s11426-019-9624-x

1 Introduction

Ceria (CeO_2)-based materials are widely used in industries such as catalysis [1–4], fuel cells [5–8], gas sensors [9], and particularly lie at the heart of the three-way catalysts (TWCs) as the Ce ions can easily switch between Ce^{4+} and Ce^{3+} driven by oxygen chemical potential [10]. Compared with their counterparts, one-dimensional (1D) ceria nanomaterials are more reactive [11–18]. Because they are usually synthesized under unusual conditions, and some reactive crystal planes may be obtained. Activity of ceria nanomaterials at high temperature is closely associated with the changes of morphology, structure and chemical states at the microscopic scale. Significant sintering of ceria nanoparticles at high temperature or the transition from cubic structure to hexagonal structure will degrade the chemical activity of ceria nanoparticles [19–24]. Moreover, defects of cerium oxide at high temperature are of great significance for the study of materials properties. Cerium oxides tends to create anion deficiencies because of the fluorite structure and the electronic configuration ([Xe]4f15d16s2) of Ce atom [25]. Esch and co-workers [26] show linear clusters of oxygen vacancies form at higher temperatures on cerium oxide, which may be important in stabilizing CeO_2-supported transition metal catalysts against sintering, and are a potentially potent surface site for catalysis and photocatalysis.

In our work, combined with the advanced *in situ* transmission electron microscopy (TEM) heating and aberration-corrected TEM technique, ceria nanowire defects during heating process are studied and much needed atomic-level

*Corresponding authors (email: khliu@pku.edu.cn; xdbai@iphy.ac.cn)

structural detail is provided. In high vacuum TEM chamber, defects appear and grow up while elevating temperature, and then the morphological shape of rhombus or hexagon is formed at 1,023 K. The mechanism for defect formation is speculated to be the release of lattice oxygen and the volatilization of surface Ce ions. Meanwhile, the more active reaction sites are introduced.

2 Experimental

The ceria nanowires are prepared by a hydrothermal method [11,13]. $Ce(NO_3)_3 \cdot 6H_2O$ (1.5 g) and NaOH (15.4 g) are dissolved in 5 and 35 mL of deionized water, respectively. Then these two solutions are mixed and keep stirring for 30 min with the formation of a milky slurry. Subsequently, this mixture is transferred into a 50-mL Teflon bottle. The Teflon bottle with this mixture is held in a stainless steel vessel autoclave, and the autoclave is sealed tightly. Finally, the autoclave is transferred into a muffle furnace, and is subjected to hydrothermal treatment at 395 K for 72 h. After the hydrothermal treatment, fresh white precipitates are separated by centrifugation, washed with deionized water and ethanol several times to remove the possible ionic remnants, and then dried at 335 K and calcined at 625 K for 4 h. The products after calcining are yellow powers.

The *in situ* TEM experiments are carried out at 300 kV in a JEM-ARM300F aberration-corrected electron microscope with vacuum of 5×10^{-6} Pa. Ceria nanowires are dispersed over silicon nitride grids and loaded into an *in situ* TEM heating holder (Zeptools Technologhy Co.), with which temperatures of the samples can be changed between 298 to 1,375 K. The applications of *in situ* TEM method have been previously reported [27–31]. Electron energy loss spectrum (EELS) is acquired with GATAN GIF 965 equipped with Dual EELS function, which can acquire the low-loss and high-loss spectrum at the same time for accurate chemical shift measurement. Since the valence of Ce ions is sensitive to the electron beam irradiation [32,33], the lower electron dose is selected to rule out the beam irradiation effect.

3 Results and discussion

3.1 Formation of defects during heating

Figure 1(a, b) shows TEM images of synthesized ceria nanowires with the size of 450–1,500 nm in length and 15–25 nm in diameter. Selected-area electron diffraction (SAED) pattern in Figure 1(c) confirms ceria nanowires can be indexed to the pure fluorite cubic structures (space group *Fm*3*m*). Figure 1(d) shows a high-resolution TEM (HRTEM) image of one typical CeO_2 nanowire. The surface bright contrast of ceria nanowire is very uniform and the lattice

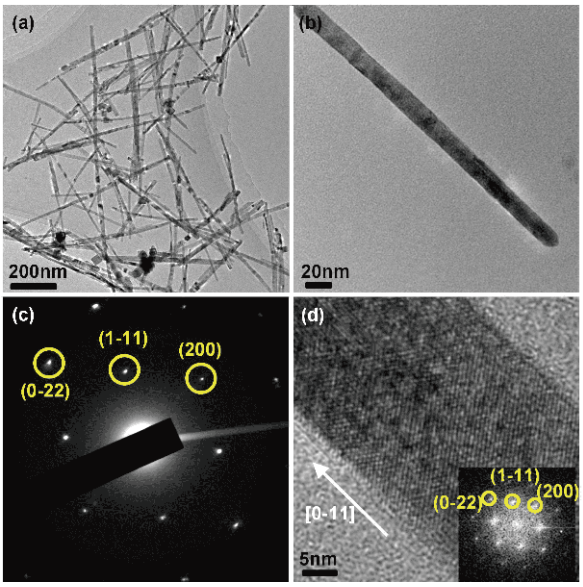

Figure 1 (a) TEM image of synthesized ceria nanowires. (b) TEM image of single ceria nanowire. (c) SAED pattern of a single ceria nanowire. Zone axis is [011]. (d) HRTEM image of a single ceria nanowire. Inset: the corresponding FFT result. Zone axis is [011] (color online).

fringe is very clear. All these indicate the prepared ceria nanowires have good crystallinity. Lower right inset shows the corresponding fast Fourier transform (FFT) result with a [011] zone axis, indicating the preferential growth direction is [0–11].

Ceria nanowires are heated and an interesting phenomenon emerges during the heating process. As the temperature is elevated, defects begin to appear in ceria nanowire and gradually grow into the regular shapes. Morphology evolution at 923, 973 and 1,023 K are shown in Figure 2(a–c), respectively. At 923 K, many areas with different bright contrast compared with the matrix can be observed on the ceria nanowire (Figure 2(a)). The initial complete single ceria nanowires should have very uniform bright contrast in TEM image, so the area with different bright contrast from the matrix suggests the defects appear on the ceria nanowire. At 973 K, the smaller defect regions coalesce, and the area size becomes larger (Figure 2(b)). At 1,023 K, the defects begin to have regular shape, as shown in Figure 2(c). Corresponding FFT result of Figure 2(c) shows no satellite diffraction spots of cubic super-structures are observed and the structure of cubic fluorite of ceria nanowires remains unchanged at 1,023 K, as shown in Figure 2(d). No phase transition occurs during heating process, which should be related to the partial pressure of oxygen and the heating temperature in the experiment [10,34].

Figure 3 shows the high angle annular dark-field scanning TEM (HAADF-STEM) image of ceria nanowires at 1,023 K, in which each bright spot represents a Ce atom column, and O atom columns cannot be seen due to their low contrast

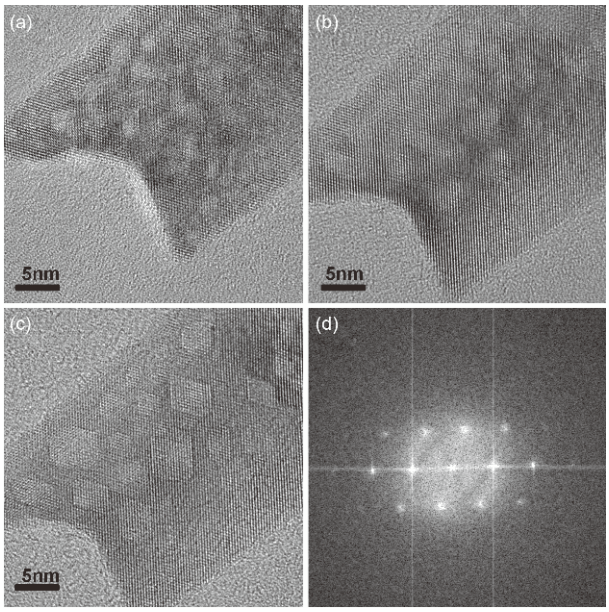

Figure 2 HRTEM images of same one ceria nanowire during *in situ* heating process. (a) HRTEM image of ceria nanowire at 923 K. (b) HRTEM image of ceria nanowire at 973 K. (c) HRTEM image of ceria nanowire at 1,023 K. (d) Corresponding FFT result of (c). Zone axis is [011].

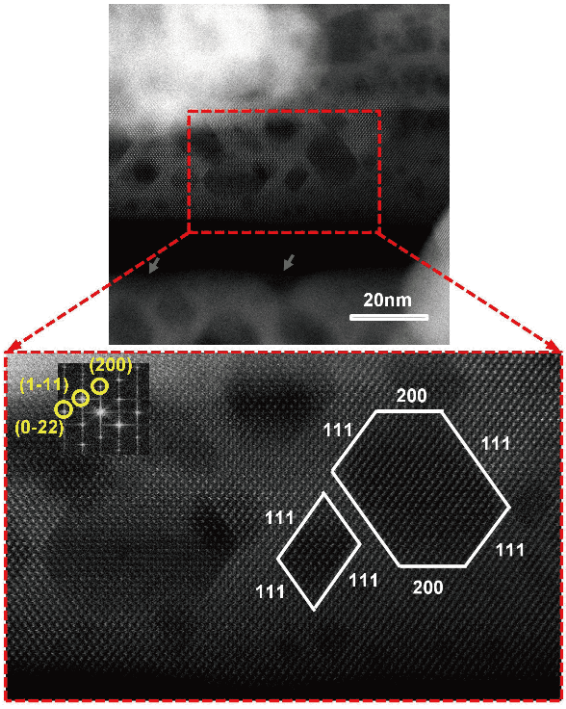

Figure 3 HAADF-STEM image of ceria nanowire at 1,023 K. Green arrows indicate the defects on the ceria nanowire edge. The enlarged image of red rectangular box is shown on bellow. Inset: the corresponding FFT result, zone axis [011]. All defective areas are surrounded by {111} and {200} planes (color online).

[35,36]. The defects can be observed on the edge of ceria nanowires, marked by green arrows in Figure 3, which suggests the defects are formed on the surface of ceria nanowires, not formed inside the nanowires. Compared with non-defective area, the lower brightness in the defective pattern demonstrates the number of Ce ions in the defective region is lower than that in the non-defective region, which suggests the formation of defective pattern is due to the volatilization of Ce ions on the nanowire surface at high temperature. The view direction is along [011] zone axis. The atomic resolution HAADF image and corresponding FFT image reveal that both defective area and non-defective area keep fluorite cubic structure, and the defective area is enclosed by well-defined {111} and {200} planes. It is well known that there are three low-index planes in the ceria fluorite cubic structure, namely the stable and neutral {111} plane, the less stable {200} plane and the higher-energy {220} plane [37,38]. Thus, defective area is surrounded by {111} and {200} planes with lower surface energy to keep overall energy more lower and crystal structure more stable. This may be the reason why the defect area exhibits a rhombic or hexagon pattern.

Oxidation state of Ce can be determined by measuring the integrated peak intensity radio of M_5/M_4 in electron energy loss spectrum (EELS). This approach works well for the previous [31,39,40]. Figure 4 shows the variation of Ce oxidation state in ceria nanowires during heating. The initial oxidation state of Ce is ~3.9 at room temperature, and then it decreases during heating process, which indicates the release of lattice oxygen and the reduction of Ce ions as the temperature is elevated.

In the HAADF-STEM image, the regular-shaped defects with different brightness can be observed when the temperature is up to 1,023 K, as shown in Figure 5(a). We use the number 1 to mark one of the high brightness defects and the number 2 to mark one of the low brightness defects. The Ce-$M_{4,5}$ edges of EELS obtained from defect 1 and defect 2 are displayed in Figure 5(b), respectively. The reference EELS for Ce^{3+} and Ce^{4+} are also given in the upper part of Figure 5 (b). The main maxima of Ce^{4+} EELS are at 884 and 902 eV, while those of Ce^{3+} are at 882 and 900 eV. And there is a reversal in the intensity of Ce-$M_{4,5}$ white lines between reference EELS of Ce^{3+} and Ce^{4+} [32]. And there is a disappearance of the shoulder in Ce^{3+} EELS compared with Ce^{4+} (arrowhead at Ce^{4+} EELS in Figure 5(b)), which suggests the strong covalent hybridization between Ce 4f and O 2p states disappears [41]. Compared with the reference EELS of Ce^{4+} and Ce^{3+}, it can be concluded that the reducibility of defect 2 is higher than that of defect 1. Thus there are differences in reducibility between different defect regions, implying that the defect degree of different defect regions is different.

Based on the above analysis, we infer that the formation of defects during heating process can be interpreted in terms of lattice oxygen release and surface cerium ions volatilization. Neutron power diffraction and reverse Monte Carlo model-

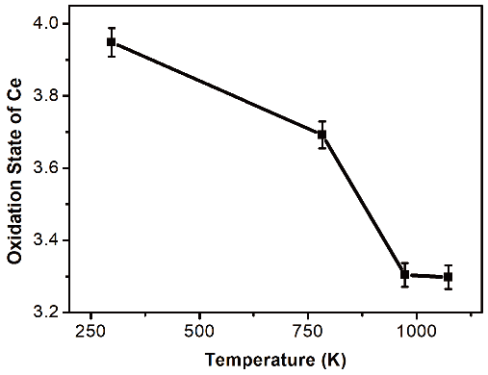

Figure 4 Ce oxidation states are plotted as a function of temperature determined by EELS analysis of the M_5/M_4 ratios for ceria nanowires.

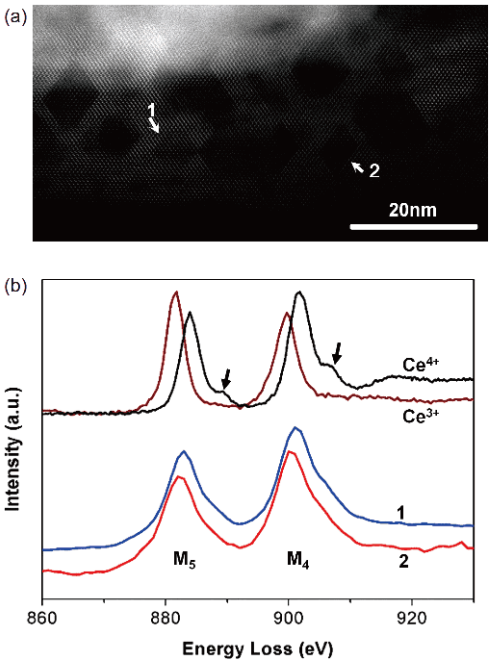

Figure 5 (a) HAADF-STEM image of ceria nanowire at 1,023 K; (b) EELS from defect 1 and defect 2 indicated on HAADF-STEM image together with reference spectra for Ce^{3+} and Ce^{4+} (color online).

ling show that, at high temperature and low partial pressure of oxygen, oxygen vacancies in ceria preferentially align as pairs in the <111> cubic directions as the degree of non-stoichiometry increases [42]. Thus in our *in situ* heating experiment, at high temperature (923 K), more atoms have enough thermal energy to overcome the diffusion barrier, and surface oxygen is more likely to escape, producing more oxygen vacancies and the cerium ions on or near the surface also be removed. Thus some defects can be form on ceria surface. As the temperature increases, the oxygen ions and cerium ions on the surface continue to volatilize and the defects region coalesce and the area become larger. When temperature reaches 1,023 K, oxygen vacancies move and completely preferentially align as pairs in the <111> cubic directions. Thus the (110) crystal planes have vast oxygen vacancies and become extremely unstable. With the volatilization of cerium ions at high temperature, the more stable (111) and (100) planes have been revealed on the ceria surface, resulting in the formation of rhombic or hexagon pattern defects surrounded by {111} and {100} planes.

3.2 Chemical characteristics of defect interface

We further investigate the interface between defective and non-defective region at 1,023 K temperature by using the STEM-EELS spectrum imaging (STEM-EELS SI) technique, which can provide a data cubes containing x and y spatial information and EELS spectral information by stepping a focused electron probe from one pixel to the next [43,44]. In Figure 6, a defect is scanned at 1,023 K. A 30×30 pixel spectrum image (indicated by the white rectangle) is acquired from the defect. In each pixel, the Ce $M_{4,5}$ edge spectrum is supposed to be a linear combination of the Ce^{3+} and Ce^{4+} signals [25,45]. By fitting the acquired spectrum in each pixel to reference spectra of Ce^{3+} and Ce^{4+} using multiple linear least-squares fitting (MLLS fitting) [46], the maps for Ce^{3+} and Ce^{4+} are obtained, as displayed in Figure 6 (b, c), respectively. A color map overlaying the Ce^{3+} and Ce^{4+} maps is shown in Figure 6(d). It is obvious that the ratio of Ce^{3+} ions is higher within the defect. The presence of Ce^{3+} in cerium oxide means the existence of oxygen vacancy, which is widely considered to have high reducibility and reactivity and is the active site of catalytic reaction [47]. Therefore, the higher Ce^{3+} ion ratio within the defect means there will be higher reducibility and reactivity here. As shown in Figure 6 (a), the bright contrast inside the defect is not uniform, which means that the surface of the defect is not completely flat and there are steps. Correspondingly, as shown in Figure 6(d), the reducibility in the defects is not uniform, as well. The Ce-$M_{4,5}$ edge EELS signals from three regions (A–C) indicate in Figure 6(d) are displayed in Figure 6(e). From the peak position of Ce-$M_{4,5}$ edge, it is clear that the order of reduction ability is: A<B<C, which means that the reduction ability of non-defective region is smaller than that of defect region, and the reduction ability of region B inside defect is smaller than that of region C. Furthermore, in Figure 6(b), more Ce^{3+} ions seem to be concentrated at the defect interface. To investigate chemical characteristic of defect interface, similar scans are performed on defect using smaller scan steps.

In Figure 7, a typical (111) defect interface is scanned at 1,023 K. A 22×18 pixel spectrum image is acquired, indicated by the white rectangle in Figure 7(a). Figure 7(b) is the enlarged image of the SI scan region. The position where an intensity profile is taken across the defect interface is indicated by the blue rectangle in the figure. The corresponding intensity profile is shown in Figure 7(f). The maps for Ce^{3+} and Ce^{4+} are shown in Figure 7(c, d), respectively. A

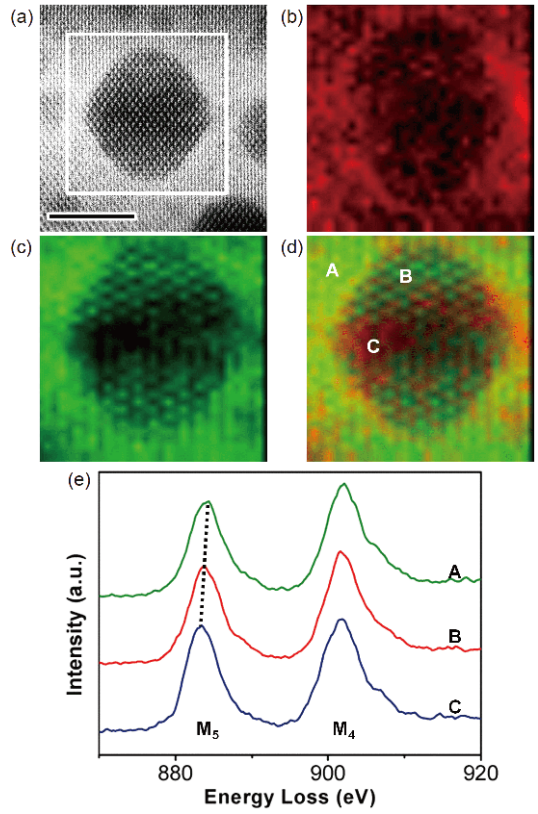

Figure 6 (a) HAADF-STEM survey image at 1,023 K showing the scanned defect and the 30×30 pixel SI scan region. Scale bar is 5 nm. (b) Ce^{3+} map (red). (c) Ce^{4+} map (green). (d) Color map with Ce^{3+} (red) and Ce^{4+} (green). (e) Ce-$M_{4,5}$ spectra from regions A–C indicated on the color map image (color online).

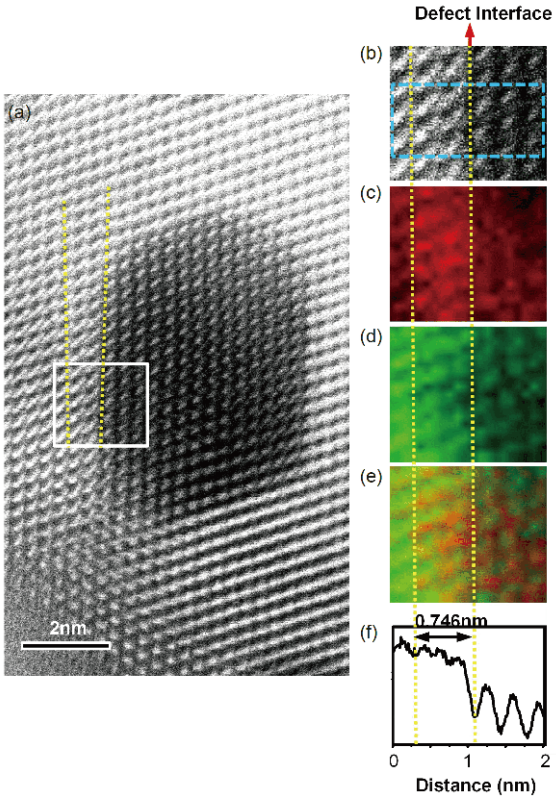

Figure 7 (a) HAADF-STEM survey image at 1,023 K showing the scanned defect and the 22×18 pixel SI scan region; (b) the enlarged image of the SI scan region in (a); (c) Ce^{3+} map (red); (d) Ce^{4+} map (green); (e) color map with Ce^{3+} (red) and Ce^{4+} (green); (f) intensity profile taken across the defect interface over the region indicated by a blue box in (b) (color online).

color map overlaying the Ce^{3+} and Ce^{4+} maps is shown in Figure 7(e). From Figure 7(b–f), the defect interface is indicated by the yellow dotted line on the right. It is obvious from the Ce^{3+} map that, closely near the defect interface, a few of atomic layers on the non-defect region have a high concentration of Ce^{3+} ions (indicated by yellow dotted line on the left), implying higher reducibility and reactivity here. The sum thickness of these atomic layers is about 0.746 nm, approximately 2.38 times as thick as the interplanar spacing of (111) crystal planes. The spacing of (111) plane is 0.314 nm. In Figure 7(a), a dislocation in the non-defect area above the scanned region can be seen, indicated by the yellow dotted lines, which leads to lattice distortion. Therefore, the sum thickness of the high reactive atomic layers at the defect interface is not an integer multiple of (111) interplanar spacing.

4 Conclusions

In summary, we study the atomic processes of defect formation and evolution ceria nanowires under heating by *in situ* Cs-TEM method. As the heating temperature increases, reduction of ceria nanowires occurs, and then defects appear on ceria nanowires, and grow into regular rhombic or hexagon shapes at 1,023 K. In order to understand microscopic structure of the defects, we analyze the atomic resolution HAADF images and STEM-EELS spectrum images of ceria nanowires at 1,023 K. No phase transition takes place both in defective area and non-defective area, which still maintain cubic fluorite structure when the temperature is up to 1,023 K. The defective area is enclosed by low-index planes—{111} and {200} planes, to keep the total energy lowest and the structure most stable. The reducibility between different defect regions is different. Within the defect, the reducibility is not uniform. At the defects interface, about 2 to 3 atomic layers on the non-defect region, close to the interface, have higher reactivity. Based on our observations, although the defects are generated due to high temperature (up to 1,023 K), the structure of cubic fluorite remains unchanged and more reactive sites are introduced. This work provides a useful insight into designing ceria-based catalyst and ionic conductors.

Acknowledgements This work was supported by the Program from Chinese Academy of Sciences (ZDYZ2015-1, XDB30000000,

XDB07030100, Y8K5261B11), the National Natural Science Foundation of China (21773303, 21872172, 51472267, 51672007, 221322304, 11290161, 51572233, 61574121, 51421002), the National Key Research and Development Program (2016YFA0300804, 2016YFA0300903), and the National Program for Thousand Young Talents of China.

Conflict of interest The authors declare that they have no conflict of interest.

Supporting information The supporting information is available online at http://chem.scichina.com and http://link.springer.com/journal/11426. The supporting materials are published as submitted, without typesetting or editing. The responsibility for scientific accuracy and content remains entirely with the authors.

1 Trovarelli A. *Catal Rev*, 1996, 38: 439–520
2 Zhou Z, Harold MP, Luss D. *Appl Catal B-Environ*, 2019, 240: 79–91
3 Aysu T, Fermoso J, Sanna A. *J Energy Chem*, 2018, 27: 874–882
4 Yang C, Li Q, Xia Y, Lv K, Li M. *Appl Surf Sci*, 2019, 464: 388–395
5 Steele B. *Solid State Ion*, 2000, 129: 95–110
6 Park S, Vohs JM, Gorte RJ. *Nature*, 2000, 404: 265–267
7 Deluga GA, Salge JR, Schmidt LD, Verykios XE. *Science*, 2004, 303: 993–997
8 Jaiswal N, Tanwar K, Suman R, Kumar D, Upadhyay S, Parkash O. *J Alloys Compd*, 2019, 781: 984–1005
9 Liao L, Mai HX, Yuan Q, Lu HB, Li JC, Liu C, Yan CH, Shen ZX, Yu T. *J Phys Chem C*, 2008, 112: 9061–9065
10 Bevan DJM, Kordis J. *J Inorg Nucl Chem*, 1964, 26: 1509–1523
11 Zhou K, Wang X, Sun X, Peng Q, Li Y. *J Catal*, 2005, 229: 206–212
12 Lin KS, Chowdhury S. *Int J Mol Sci*, 2010, 11: 3226–3251
13 Mai HX, Sun LD, Zhang YW, Si R, Feng W, Zhang HP, Liu HC, Yan CH. *J Phys Chem B*, 2005, 109: 24380–24385
14 Boucher MB, Goergen S, Yi N, Flytzani-Stephanopoulos M. *Phys Chem Chem Phys*, 2011, 13: 2517–2527
15 Yi N, Si R, Saltsburg H, Flytzani-Stephanopoulos M. *Energy Environ Sci*, 2010, 3: 831–837
16 Lu X, Zhai T, Cui H, Shi J, Xie S, Huang Y, Liang C, Tong Y. *J Mater Chem*, 2011, 21: 5569–5572
17 Tang ZR, Zhang Y, Xu YJ. *RSC Adv*, 2011, 1: 1772–1777
18 Yu XF, Mao LB, Ge J, Yu ZL, Liu JW, Yu SH. *Sci Bull*, 2016, 61: 700–705
19 Perrichon V, Laachir A, Bergeret G, Fréty R, Tournayan L, Touret O. *J Chem Soc Faraday Trans*, 1994, 90: 773–781
20 Xiao W, Guo Q, Wang EG. *Chem Phys Lett*, 2003, 368: 527–531
21 Bunluesin T, Gorte RJ, Graham GW. *Appl Catal B-Environ*, 1997, 14: 105–115
22 Mamontov E, Egami T, Brezny R, Koranne M, Tyagi S. *J Phys Chem B*, 2000, 104: 11110–11116
23 Mikulová J, Rossignol S, Barbier Jr. J, Duprez D, Kappenstein C. *Catal Today*, 2007, 124: 185–190
24 Hsiao WI, Lin YS, Chen YC, Lee CS. *Chem Phys Lett*, 2007, 441: 294–299
25 Wang ZL, Kang ZC. *Functional and Smart Materials: Structural Evolution and Structure Analysis*. *Volume 4: Fluorite-Type and Related Structure Systems*. New York: Plenum Press, 1998. 151–177
26 Esch F, Fabris S, Zhou L, Montini T, Africh C, Fornasiero P, Comelli G, Rosei R. *Science*, 2005, 309: 752–755
27 Huang Q, Wang L, Xu Z, Wang W, Bai X. *Sci China Chem*, 2018, 61: 222–227
28 Wei JK, Xu Z, Wang H, Wang WL, Bai XD. *Sci China Tech Sci*, 2016, 59: 1080–1084
29 Tang M, Zhu B, Meng J, Zhang X, Yuan W, Zhang Z, Gao Y, Wang Y. *Mater Today Nano*, 2018, 1: 41–46
30 Epicier T, Aouine M, Cadete Santos Aires FJ, Massin L, Gélin P. *Microsc Microanal*, 2018, 24: 1648–1649
31 Crozier PA, Wang R, Sharma R. *Ultramicroscopy*, 2008, 108: 1432–1440
32 Garvie LAJ, Buseck PR. *J Phys Chem Solids*, 1999, 60: 1943–1947
33 Gao P, Kang Z, Fu W, Wang W, Bai X, Wang E. *J Am Chem Soc*, 2010, 132: 4197–4201
34 Adachi G, Imanaka N. *Chem Rev*, 1998, 98: 1479–1514
35 Hartel P, Rose H, Dinges C. *Ultramicroscopy*, 1996, 63: 93–114
36 Pennycook SJ, Rafferty B, Nellist PD. *Microsc Microanal*, 2002, 6: 343–352
37 Wang ZL, Feng X. *J Phys Chem B*, 2003, 107: 13563–13566
38 Zhang F, Jin Q, Chan SW. *J Appl Phys*, 2004, 95: 4319–4326
39 Sharma R, Crozier † PA, Kang ZC, Eyring L. *Philos Mag*, 2004, 84: 2731–2747
40 Manoubi T, Colliex C, Rez P. *J Electron Spectrosc Relat Phenom*, 1990, 50: 1–18
41 Finazzi M, de Groot FMF, Dias AM, Kappler JP, Schulte O, Felsch W, Krill G. *J Electron Spectrosc Relat Phenom*, 1996, 78: 221–224
42 Hull S, Norberg ST, Ahmed I, Eriksson SG, Marrocchelli D, Madden PA. *J Solid State Chem*, 2009, 182: 2815–2821
43 Jeanguillaume C, Colliex C. *Ultramicroscopy*, 1989, 28: 252–257
44 Hunt JA, Williams DB. *Ultramicroscopy*, 1991, 38: 47–73
45 Turner S, Lazar S, Freitag B, Egoavil R, Verbeeck J, Put S, Strauven Y, Van Tendeloo G. *Nanoscale*, 2011, 3: 3385–3390
46 Tan H, Turner S, Yücelen E, Verbeeck J, Van Tendeloo G. *Phys Rev Lett*, 2011, 107: 107602
47 Campbell CT, Peden CHF. *Science*, 2005, 309: 713–714